Advances in
Bridge Engineering

Blast resistance of CFRP composite strengthened masonry arch bridge under close-range explosion

Amin Bagherzadeh Azar[1*] and Ali Sari[2]

*Correspondence:
azar19@itu.edu.tr

[1] Institute of Earthquake Engineering and Disaster Management, Istanbul Technical University, ITU Ayazaga Campus, Maslak, Istanbul 34469, Turkey
[2] Faculty of Civil Engineering, Istanbul Technical University, ITU Ayazaga Campus, Maslak, Istanbul 34469, Turkey

Abstract

Carbon fiber reinforced polymers (CFRP) are recognized for their exceptional strength-to-weight ratio. They offer a viable and effective solution for strengthening and retrofitting masonry bridges, helping to extend their service life, improve structural performance, and meet modern safety and load requirements. Wrapping of CFRP around masonry elements can enhance their confinement and ductility. This flexibility plays a crucial role in preventing sudden brittle failure, allowing for controlled deformation, which is essential for blast resistance. Additionally, CFRP materials possess the ability to flex and absorb energy, which proves beneficial in containing and redistributing forces generated during an explosion, consequently reducing the risk of catastrophic failure. This study employed the coupled Eulerian–Lagrangian (CEL) technique available in the finite element software Abaqus/Explicit to simulate the blast loads. Various detonation scenarios were considered, taking into account factors such as location and their impacts on bridge structures. A detailed micro-model was developed using finite element software and accurate geometric data acquired from FARO laser scanning of the case study. The properties of masonry units and backfill were characterized using the Johnson-Holmquist II damage model and Mohr–Coulomb criteria. The Jones-Wilkins-Lee equation of state (EOS) was applied to replicate the behavior of trinitrotoluene (TNT). In accordance with the JH-II model, the researchers formulated a VUMAT code. The study examined the distinct damage mechanisms and overall structural responses of bridges. By evaluating the blast resistance of individual bridge models, the most critical scenarios were pinpointed. Carbon Fiber Reinforced Polymer (CFRP) was then utilized as a method to fortify bridges against blast loads. A comparison was made between the damage propagation before and after the reinforcement.

Keywords: Blast wave, Strengthening method, Masonry bridge, Collapse, CFRP

1 Introduction

Bridges are frequently subjected to deliberate or accidental explosions due to their status as iconic landmarks, vital transportation pathways, and representations of national or cultural importance. The destruction of a bridge can results in not only physical harm but also have a deep psychological impact. Depending on the magnitude of the explosions, bridges may sustain considerable structural harm, potentially leading to partial or

complete collapse. Therefore, it is imperative to reinforce masonry bridges to ensure their durability, safety, and ability to withstand changing environmental, traffic, and safety demands. Through the implementation of suitable reinforcement methods, authorities can effectively oversee and safeguard critical infrastructure assets, benefiting both communities and economies. The utilization of Carbon Fiber Reinforced Polymers (CFRP) for strengthening masonry bridges is recognized as a contemporary, proficient, and long-lasting method for retrofitting. This approach addresses structural deficiencies, improves resilience against seismic events, and prolongs the lifespan of critical infrastructure. As infrastructure ages and encounters new challenges, CFRP remains a favored option for sustainable and efficient bridge strengthening initiatives globally. CFRP materials, known for their lightweight yet robust properties, offer substantial tensile strength when applied to masonry structures. This reinforcement plays a vital role in augmenting the load-carrying capacity of the bridge, enabling it to endure higher stresses and loads (Kadhim et al. 2020). CFRP can be tailored and applied to different shapes and sizes of masonry elements, including arches, columns, and walls. Its flexibility makes it suitable for retrofitting existing structures without significantly altering their appearance or historical character. Moreover, Carbon Fiber Reinforced Polymer (CFRP) exhibits non-corrosive properties, contrasting with conventional steel reinforcements that are prone to corrosion in masonry constructions over time (Wang et al. 2018). This attribute contributes to the prolonged durability of bridges and a decrease in maintenance expenses. Studies have demonstrated that the reinforcement with CFRP significantly contributes to the blast resistance of masonry arches by mitigating shearing cracks and spalling, reducing dynamic deformations in the arch structure, and enhancing overall structural stability (Effiong and Ede 2022; Tiwary et al. 2022). Carbon fiber reinforced polymers (CFRPs) have found extensive applications across diverse domains within civil engineering. Accurate estimation of CFRP material strain and the compressive strength of masonry units is crucial as it directly impacts the effectiveness of reinforcement. (Milad et al. 2022) investigated the efficacy of three established ensemble machine learning models in computer science to optimize the CFRP composite strain enhancement ratio. The research presented a dependable and resilient approach for enhancing the composite material. (Chen et al. 2022) conducted an assessment of the axial compressive constitutive model for CFRP confined circular concrete columns and developed a prognostic model for the axial compressive mechanical characteristics of CFRP-confined concrete structures. CFRP lattices are constructed using continuous fiber that are arranged longitudinally and transversely to form lattices through a specialized procedure, followed by drying and shaping through resin infiltration. (Liu et al. 2021a) conducted a study where they applied sprayed polyurea with FRP grid to strengthen concrete arch members. The study examined different application methods, including spraying solely on the inner side of the arch, spraying on the entire arch surface, and spraying on the inner side of the arch with FRP grid. Through blast testing, it was observed that damage patterns such as cracking, spalling, and crushing of the concrete on the arch occurred successively as the proportional distance decreased. Subsequently, a quasi-static midspan concentrated load test was conducted to evaluate the residual bearing capacity of the arch post-blast, providing a quantitative assessment of the extent of damage. The findings indicated that the sprayed polyurea coating exhibited

superior spalling resistance compared to the traditional method of applying FRP, significantly enhancing the blast resistance of concrete arches. (Zhang et al. 2020) conducted a comprehensive review on the response of reinforced concrete (RC) structural members to blast loads. Their study included a tabulated collection of data on the impact of various parameters on the blast response of RC columns, the effectiveness of different retrofitting techniques in mitigating damage to RC columns under blast loads, the influence of different parameters on the blast resistance of retrofitted columns, and a summary of modeling considerations in previous analytical studies. (Siba 2014) carried out an experimental study investigating the impact of close-in explosions on RC columns with varying transverse reinforcement details at different scaled distances. The study examined three types of test specimen columns: conventional, seismic, and prestressed columns. The prestressed columns were specifically designed to replicate the effects of axial load in addition to their own weight. (Yan et al. 2020; Hu et al. 2021) conducted a numerical study to explore techniques for improving the capacity of reinforced concrete (RC) columns. (Huang et al. 2021) conducted a unique investigation to analyze the impact of axial compression ratio, torsional-bending ratio, and eccentricity on the load-carrying capacity of RC columns reinforced with high-performance ferrocement laminate (HPFL)-bonded steel plates (BSP) under combined loading conditions. The researchers observed that all strengthened specimens subjected to combined loading showed an increase in load-carrying capacity, although there was a significant reduction in energy absorption capacity and ductility ratios. (Dong et al. 2020) developed a computational model to examine the response of reinforced concrete (RC) columns retrofitted with various fiber-reinforced polymer (FRP) composites, including carbon fiber-reinforced polymer (CFRP), glass fiber-reinforced polymer (GFRP), and aramid fiber-reinforced polymer (AFRP), subjected to blast loads. The study found that among the three types of FRP, CFRP demonstrated superior performance in enhancing the blast resistance capacity of RC columns. Furthermore, the authors noted that a full retrofitting approach yielded the most effective blast load resistance compared to other retrofitting methods. In a related study, (Xu et al. 2020) conducted experimental research on the impact behavior of cantilevered CFRP-strengthened RC columns, demonstrating an enhancement in lateral impact resistance. (Swesi et al. 2022) experimentally investigated the performance of CFRP-strengthened RC columns subjected to impact loads and showed positive effects when the number of CFRP layers increased. (Liu et al. 2021b) conducted both experimental and numerical investigations into the impact responses of circular reinforced concrete (RC) columns strengthened with carbon fiber-reinforced polymer (CFRP), and conducted parametric analyses to evaluate the influence of various structural and loading factors on the performance of the columns. (Ali et al. 2021) performed numerical simulations on a cable-stayed bridge under blast loading conditions, focusing on the efficacy of CFRP in improving the bridge's resistance to blasts. (Iqbal et al. 2018) conducted an experimental study to assess the impact of polyurea coating on the survivability of concrete structures under blast loading, demonstrating its potential to enhance concrete blast resistance and overall performance. Polyurea shows promise as a material for engineering applications aimed at safeguarding bridges and their components against extreme loads. This paper advocates for the use of CFRP layers for the surface of the arches as a strengthening technique. The objective of this research was to assess the

efficacy of reinforcing bridges with CFRP in withstanding combined blast loads, and to analyze the impact of specific retrofit strategies on enhancing the bridges resilience. Computational models of the reinforced bridges were created using ABAQUS software to analyze the behavior of masonry bridge under different blast loads and evaluate the performance of the retrofit effectiveness in reducing the effects of air blasts.

2 Case study: halilviran bridge

The study examined the Halilviran Bridge in Turkey as a focal point. This ancient stone arch bridge features seven arches, as illustrated in Fig. 1. A comprehensive analysis of the bridge's geometric characteristics was conducted using a 3D laser scanning technique. The bridge spans 132 m in length and is 5.07 m wide, with a maximum arch span of 7.26 m and a minimum span of 5.95 m. The investigation concentrated on a specific segment of the bridge to assess the degree of structural component deterioration failures, considering the intricate micro modeling and near symmetrical design of the bridge.

3 Methodology

The Coupled Eulerian Lagrangian method plays a crucial role in blast simulation by integrating accurate modeling of fluid dynamics (Eulerian) with realistic representation of structural response and deformation (Lagrangian). This approach enables comprehensive analysis and prediction of blast effects, contributing to safer and more resilient infrastructure design and emergency planning. In blast simulation, the Coupled Eulerian Lagrangian (CEL) method is particularly advantageous due to its ability to accurately model the interaction between high-speed fluids (such as shock waves and explosive gases) and solid structures (such as buildings, vehicles, or protective barriers). The CEL method utilizes a Eulerian approach to accurately capture the propagation of shockwaves and blast pressures through the air or other fluids. In this Eulerian framework, the computational domain is typically divided into a fixed grid where fluid properties (density, pressure, velocity) are tracked as functions of time and spatial coordinates. CEL models the behavior of explosive gases, their expansion, and interaction with the surrounding medium. This includes phenomena like rarefaction waves and turbulence generated by the blast. On the other hand, the solid structures, such as buildings or vehicles, are represented using a Lagrangian approach. This involves discretizing the structure into finite elements or particles that move and deform according to the blast-induced forces and pressures they experience. The CEL can simulate complex material behaviors such as plastic deformation, fracture, and failure due to high-speed impact from blast waves. One of the key strengths of the CEL method in blast simulation is its ability to handle fluid–structure interaction robustly. This interaction is crucial for accurately predicting the structural response to blast loading, including deformation, displacement, and damage. moreover, CEL accurately computes the energy transfer between the blast wave and the affected structures. This helps in assessing the severity of damage and designing protective measures against blasts. In this research, Eulerian components were employed to model the behavior of trinitrotoluene (TNT), soil, and their surrounding context. The analysis incorporated the Johnson-Holmquist II (JH-II) and Mohr–Coulomb material models for the assessment of masonry unit and infill, respectively. The Jones-Wilkins-Lee (JWL) equation of state (EOS) was adopted to replicate the characteristics of TNT
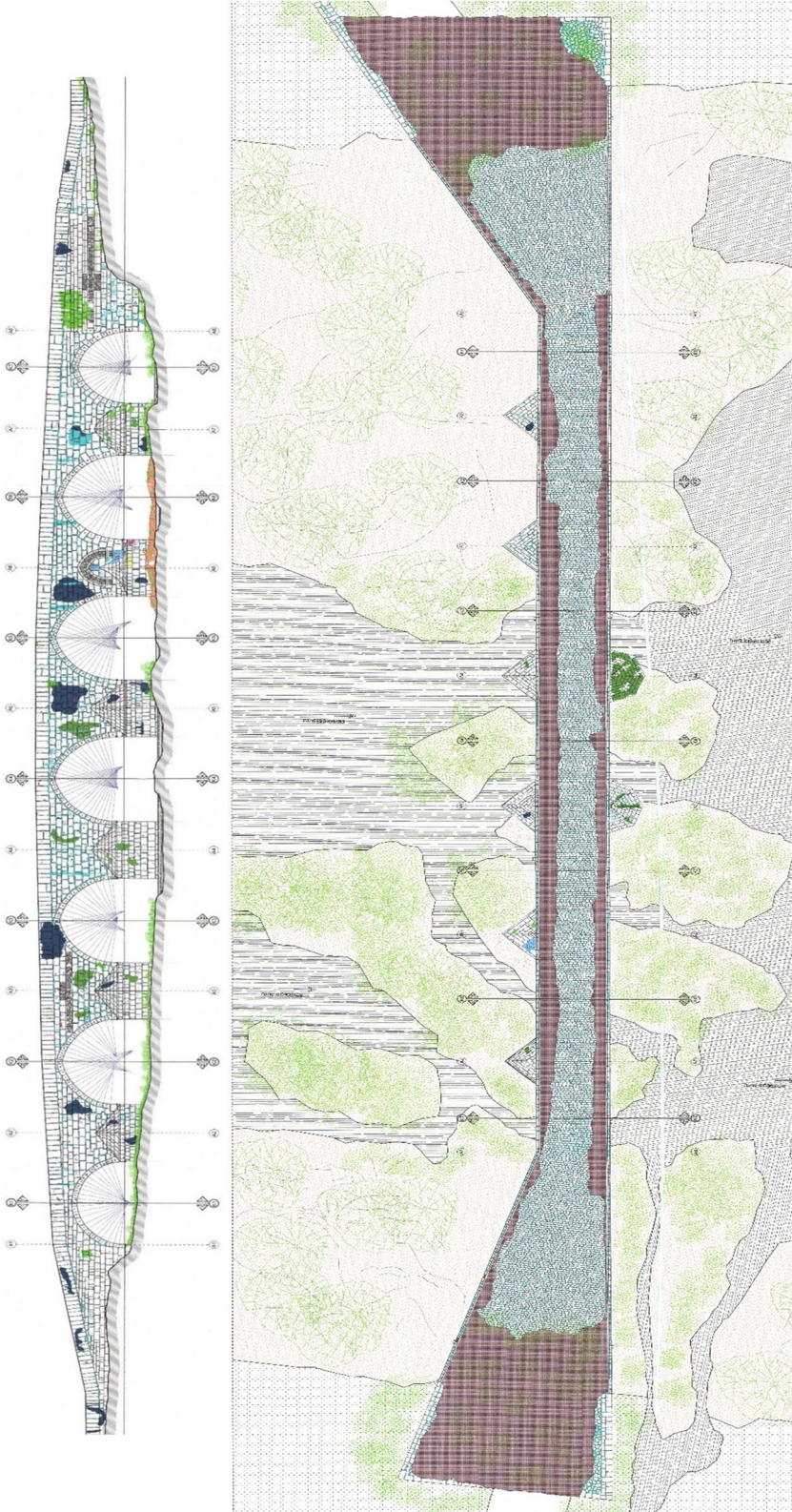
Fig. 1 Case Study (Azar and Sari 2023)

explosive substances. To confine the explosion wave generated by TNT, a cubic Eulerian domain measuring 30 m × 30 m × 30 m was established and filled with air, as depicted in Fig. 2. The study utilized eight-node reduced integration Eulerian elements (C3D8R) to represent both TNT and air. Non-reflecting boundary conditions were enforced on the Eulerian domain to prevent the reflection of the blast wave. Material flow tracking was achieved through the utilization of volume fraction, denoting the proportion of material present within the Eulerian domain.

Figure 3a,b depicted a bridge with a span of 6.26 m and a height of 8.25 m, showcasing the absence of reinforcement. The illustration also provided details regarding the geometry and composition of the mortar. In the reinforced bridge model, carbon fiber reinforced polymer (CFRP) layers were applied to the arch and piers surfaces. Both bridge models featured pinned supports at the bottom end of the side walls. Abaqus/ Explicit software incorporated general contact for Eulerian and Lagrangian elements, encompassing hard contact in the normal direction and frictionless contact in the tangential direction. A mesh sensitivity analysis was conducted to validate the model's accuracy, with results documented in Table 1. Various seed values were allocated to different regions of the model, with finer mesh refinement concentrated towards the impact point to achieve a suitably refined mesh. The study revealed that reducing the mesh size to 3 mm led to converging results while maintaining a reasonable computation time. The meshing map and characteristics of the explosives, represented as spherical objects, were delineated in Fig. 3c and the analysis timeframe were set at 50 ms.
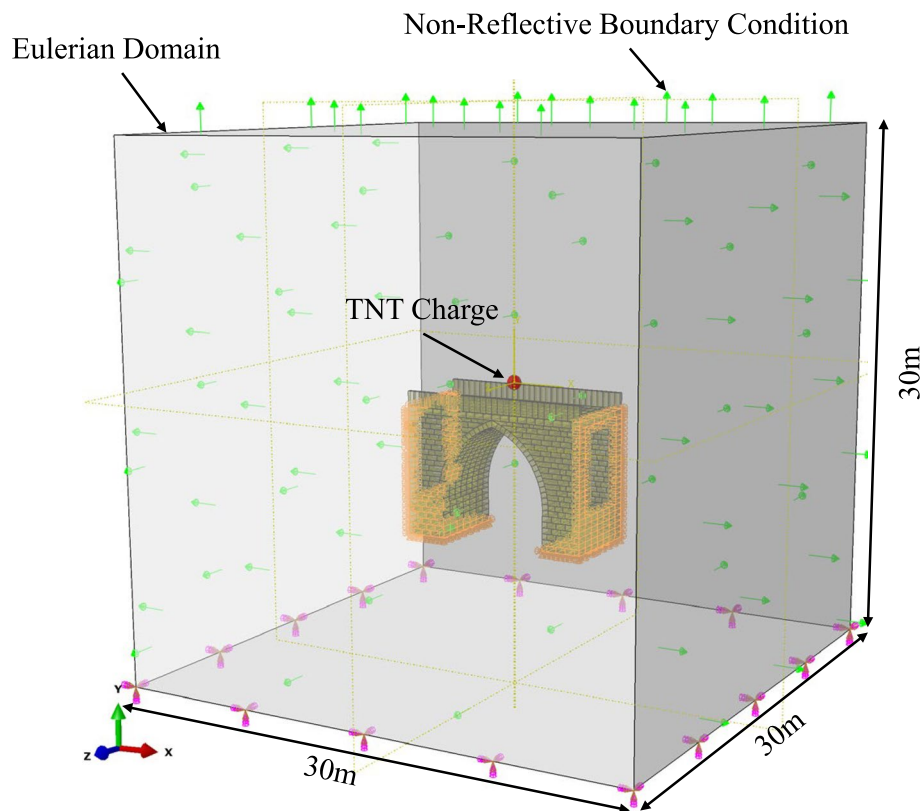

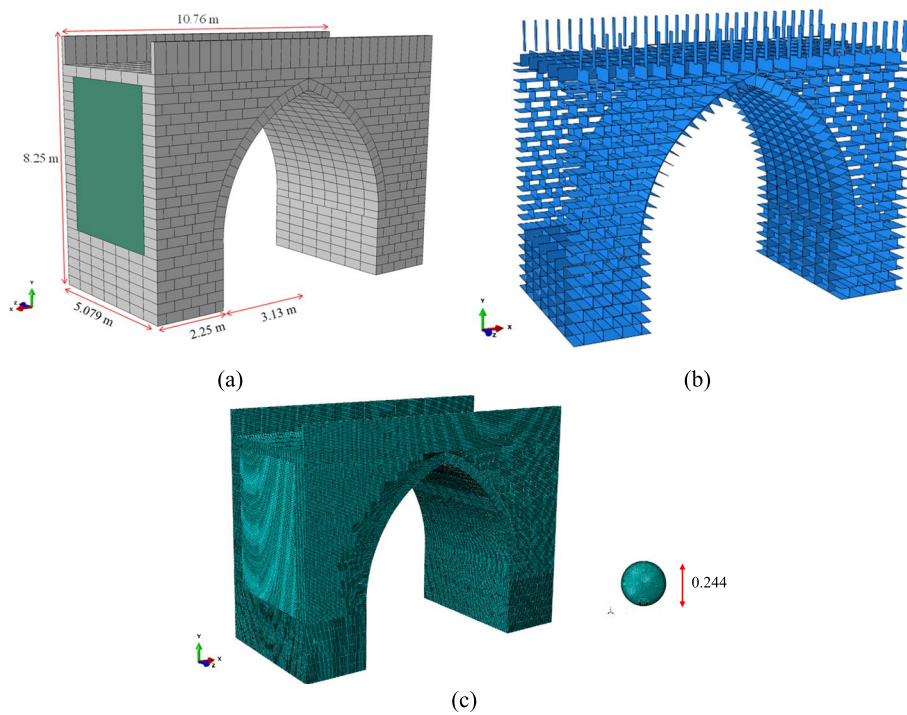**Fig. 2** Eulerian domain used for masonry bridge and TNT

Fig. 3 Bridge detail: Geometric detail (**a**), Mortar details of the bridge (**b**) and Meshing map for the simulation model (**c**)

Table 1 Mesh sensitivity analysis for blast analysis of masonry bridge

Mesh	Element size (m)	No. of elements	Deformation at the deck of the bridge (m)	Computational time (with 8 cores) (h)
Coarse	0.1	450,702	0.386	2
Fine	0.06	751,170	0.343	6
Finer	0.03	1,502,340	0.288	10
Finest	0.02	2,253,510	0.282	14

4 Governing equation and material properties

4.1 Composite failure model; damage initiation

The concept of damage initiation pertains to the commencement of deterioration at a specific location within a material. Within the Abaqus software, the criteria for damage initiation in fiber-reinforced composites are derived from Hashin's theory, as outlined in works by Hashin and Rotem (1973).These criteria encompass four distinct mechanisms for damage initiation: fiber tension, fiber compression, matrix tension, and matrix compression. The general forms of the initiation criteria are as follows:

$$\text{Fiber tension } \left(\widehat{\sigma}_{11} \geq 0\right) : F_f^t = \left(\frac{\widehat{\sigma}_{11}}{X^T}\right)^2 + \alpha \left(\frac{\widehat{\tau}_{12}}{S^L}\right)^2 \tag{1}$$

$$\text{Fiber compression } (\widehat{\sigma}_{11} < 0) : F_f^c = (\frac{\widehat{\sigma}_{11}}{X^C})^2, \tag{2}$$

$$\text{Matrix tension } (\widehat{\sigma}_{22} \geq 0) : F_m^t = (\frac{\widehat{\sigma}_{22}}{Y^T})^2 + \alpha(\frac{\widehat{\tau}_{12}}{S^L})^2 \tag{3}$$

$$\text{Matrix compression } (\widehat{\sigma}_{22} < 0) : F_m^c = (\frac{\widehat{\sigma}_{22}}{2S^T})^2 + [(\frac{Y^C}{2S^T})^2 - 1]\frac{\widehat{\sigma}_{22}}{Y^C} + (\frac{\widehat{\tau}_{12}}{S^L})^2 \tag{4}$$

$\widehat{\sigma}$ that is used to evaluate the initiation criteria and which is computed from: $\widehat{\sigma} = M\sigma$, where σ is the true stress and M is the damage operator:

$$M = \begin{bmatrix} \frac{1}{(1-d_f)} & 0 & 0 \\ 0 & \frac{1}{(1-d_m)} & 0 \\ 0 & 0 & \frac{1}{(1-d_s)} \end{bmatrix}, d_f = \begin{cases} d_f^t, if\widehat{\sigma}_{11} \geq 0, \\ d_f^c, if\widehat{\sigma}_{11} < 0, \end{cases} d_m = \begin{cases} d_m^t, if\widehat{\sigma}_{22} \geq 0, \\ d_m^c, if\widehat{\sigma}_{22} < 0, \end{cases} d_s = 1 - \left(1 - d_f^t\right)\left(1 - d_f^c\right)(1 - d_m^t)(1 - d_m^c). \tag{5}$$

The effective stress, $\widehat{\sigma}$, is intended to represent the stress acting over the damaged area that effectively resists the internal forces. Based on the HASHIN DAMAGE criteria model theory that includes state variables such as the damage initiation criteria components (DMICRT), Maximum value of the fiber tensile initiation criterion experienced during the analysis (HSNFTCRT), Maximum value of the fiber compressive initiation criterion experienced during-the analysis (HSNFCCRT), Maximum value of the matrix tensile initiation criterion experienced during the analysis (HSNMTCRT) and Maximum value of the matrix compressive initiation criterion experienced during the analysis (HSNMCCRT). Table 2 show the input parameters for the composite constant's material properties.

4.2 Jones-Wilkins-Lee equation of state

The detonation was modelling using reduced integration elements with eight nodes (EC3D8R). The Jones-Wilkins-Lee (JWL) equation of state (EOS) model is used to compute the pressure (P) for various equivalent TNT explosives, as illustrated in the following:

$$P = A\left(1 - \frac{\omega}{R_1\overline{\rho}}\right)e^{-R_1\overline{\rho}} + B\left(1 - \frac{\omega}{R_2\overline{\rho}}\right)e^{-R_2\overline{\rho}} + \omega\overline{\rho}e_{int} \tag{6}$$

Table 2 Composite constants (Bürger et al. 2012)

ρ	E_1	E_2	ν_{12}	G_{12}	G_{13}	G_{23}
1320	427E+8	427E+8	0.05	44E+8	44E+8	23E+8
X^T	X^C	Y^T	Y^C	S^L	S^T	
643E+6	267E+6	643E+6	267E+6	37E+6	37E+6	

The parameters A, B, R_1, R_2, and ω are the constants associated with TNT material. The variable $\overline{\rho}$ denotes the ratio of explosive material density to current density, while e_{int} represents the specific internal energy at atmospheric pressure. The initial two expressions refer to the high-pressure effects resulting from the explosion, whereas the third phrase pertains to the low-pressure effects caused by the significant volume reduction. Table 3 listed the material properties of the TNT explosive charge.

4.3 Constitutive model of the masonry

The study utilized ABAQUS software to analyze the stone material used in constructing the arch, parapet, and pier of a bridge model, taking into account the material's non-linear properties. Masonry arch bridges under loads tend to develop cracks, usually along mortar lines, which are fragile and can lead to structural failure. The accurate selection of a suitable material model for numerical analysis is crucial as it precisely reflects the structure's response to impact loads. ABAQUS software provides a variety of material models specifically designed for analyzing brittle materials subjected to blast forces. However, these models may not be suitable for high-strain rate scenarios, and their effectiveness diminishes when simulating structures under these loads. Therefore authors developed a VUMAT code to investigate the Johnson-Holmquist II constitutive model (Johnson and Holmquist 1999) for replicating the behavior of stone blocks. JH-II material model consist of three distinct components as follows:

4.3.1 Strength model

The Johnson-Holmquist II model is commonly used to study the mechanical properties of brittle materials. These materials are prone to gradual deterioration when subjected to dynamic stress, primarily due to the propagation of cracks. Figure 4a provided a detailed illustration of the model from three distinct perspectives. Each condition is associated with a specific strength equation that determines the ratio of normalized equivalent stress to normalized pressure. The strength of the material is expressed in terms of the normalized von Mises equivalent stress as:

$$\sigma^* = \sigma_i^* - D\left(\sigma_i^* - \sigma_f^*\right) \tag{7}$$

where σ_i^* is the normalized intact equivalent stress, σ_f^* is the normalized fractured equivalent stress, and D is the damage variable. The normalized equivalent stresses (σ^*, σ_i^* and σ_f^*) have the general form $\sigma^* = \frac{\sigma}{\sigma_{HEL}}$, where σ is the actual von Mises equivalent stress and σ_{HEL} is the equivalent stress at the Hugoniot elastic limit (HEL). The model assumes that the normalized intact and fractured stresses can be expressed as functions of the pressure and strain rate as:

Table 3 JWL-EOS parameters of trinitrotoluene

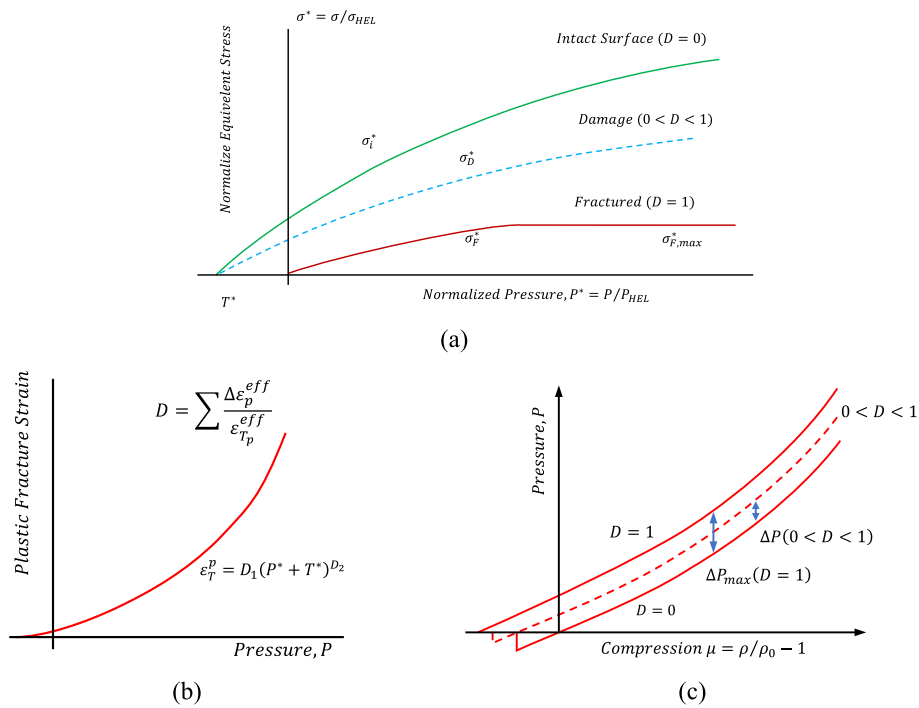| Density (ρ) Kg/m³	Detonation Wave Speed (m/s)	$A(Pa)$	$B(Pa)$	ω	R_1	R_2	Detonation Energy Density (J/Kg)
1630	6930	3738E+8	3747E+6	0.35	4.15	0.9	6,060,000

Fig. 4 JH-2 Model: (**a**) Strength graph, (**b**) Damage model and (**c**) EOS model of the Johnson-Holmquist II

$$\sigma_i^* = A(P^* + T^*)^N(1 + CLn\dot{\varepsilon}^*) \le \sigma_i^{max} \tag{8}$$

$$\sigma_i^* = B(P^*)^M(1 + CLn\dot{\varepsilon}^*) \le \sigma_f^{max} \tag{9}$$

The material parameters are A, B, C, M, N and the optional limits for the strengths σ_i^{max} and σ_f^{max}. The normalized pressure is defined as $P^* = \frac{P}{P_{HEL}}$, where P is the actual pressure and P_{HEL} is the pressure at the HEL. The normalized maximum tensile hydrostatic pressure is $T^* = \frac{T}{P_{HEL}}$, where T is the maximum tensile pressure that the material can withstand.

4.3.2 Damage model

The Fig. 4b illustrated the modified pattern of damage, demonstrating a non-linear increase. Within the equation, the variable D signified the aggregation of successive plastic deformation increments $\Delta\varepsilon_f^{pl}$:

$$D = \sum \frac{\Delta\varepsilon_f^{Pl}}{\varepsilon_f^{Pl}} \tag{10}$$

The symbol $\Delta\varepsilon_f^{Pl}$ denoted the incremental plastic strain, while ε_f^P represents the independent plastic strain, which can be expressed as follows:

$$\varepsilon_f^{Pl} = D_1(P^* + T^*)^{D_2} \tag{11}$$

The variables D_1 and D_2 denoted material constants. The plastic strain during an integration cycle, $\Delta\varepsilon_f^P$, and the plastic strain to fracture under a constant pressure, $\varepsilon_f^{Pl} = f(p)$, represented, with D_1 and D_2 serving as the damage factors for ε_f^P.

4.3.3 Equation of State (EOS)

When a material undergoes plastic deformation or damage exceeding a certain threshold, it reaches failure point characterized by a strength surpassing, resulting in behavior akin to that of a fluid as shown in Fig. 4c. At this stage, the unit became incapable of resisting any stresses, and both the hydrostatic pressure and deviatoric stress diminish to zero. The polynomial equation of state (EOS) depicted the relationship between the hydrostatic pressure (P) and the volumetric strain (μ), describes in two different stages; purely elastic and plastic damage;

$$\begin{array}{ll} P = K_1 + K_2\mu^2 + K_3\mu^3 & if \ (\mu \geq 0) \\ P = K_1\mu & if \ (\mu \leq 0) \end{array} \tag{12}$$

where $\mu = \frac{\rho}{\rho_0} - 1$. The model includes the effects of dilation or bulking that occur when brittle materials fail by including an additional pressure increment, ΔP, such that:

$$P = K_1 + K_2\mu^2 + K_3\mu^3 + \Delta P (0 < D \leq 1) \tag{13}$$

The material parameters K_1, K_2, and K_3, along with ΔP representing an additional pressure increment post-damage initiation, volumetric strain denoted by (ε), final and initial densities ρ and ρ_0 respectively, are key components in the JH-II model. The authors developed VUMAT based on this model, which includes 32 mechanical constants and 8 solution-dependent state variables. These variables include equivalent plastic strain (FEEQ), ductile damage initiation criterion (DUCTCRT), pressure increment due to bulking (DELTAP), and damage (D), among others. The input parameters for the Johnson-Holmquist II model for masonry properties are listed in Table 4.

4.4 Constitutive Model of the backfill

4.4.1 Soil

This study employed the Mohr–Coulomb constitutive model to incorporate the infill material model. The Mohr–Coulomb criteria define yielding as the point at which the shear stress at any point within a material equals a value that is linearly related to the normal stress in the same plane. The Mohr–Coulomb shear stress (τ) is contingent upon the plasticity models for stress (σ), cohesion (c), and friction (φ) and can be mathematically represented as follows:

$$\tau = c + \sigma \ tan \ \theta \tag{14}$$

Table 4 The masonry material properties

ρ(Kg/m³)	A	B	C	G(GPa)	D_1	D_2	β	σ(MPa)	K_1
2600	1.01	0.68	0.005	17.8	0.005	0.7	0.68	51	19.5
K_2	K_3	HEL(GPa)	P_{HEL}(GPa)	$\dot{\varepsilon}_0$	σ_{fmax}^*	υ	M	N	
-23	2980	4.5	2.6	1	0.2	0.2	0.83	0.83	

Table 5 Input parameters for backfill material

$\rho(Kg/m3)$	$E(N/MM^2)$	υ	$c(N/MM^2)$	$\varnothing(°)$
1900	500	0.2	0.05	20

(a) Macro-modeling   (b) Simplified micro-modeling   (c) Detailed micro-modeling
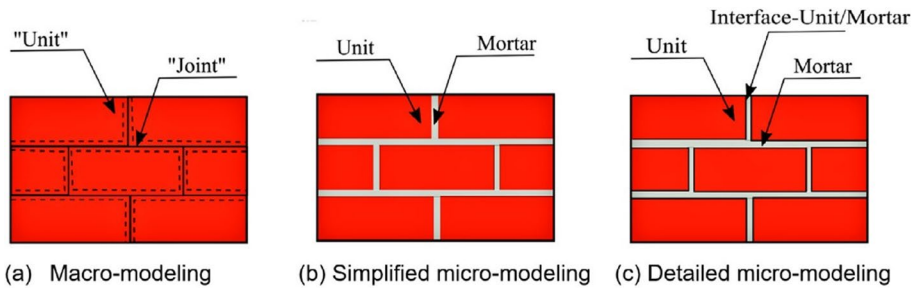
Fig. 5 Masonry mdeling

The Mohr–Coulomb model is characterized by three stress invariants, one of which is the equivalent compressive stress:

$$p = -\frac{1}{3}trace(\sigma) \tag{15}$$

The equivalent stress according to Mises:

$$q = \sqrt{\frac{3}{2}(S:S)} \tag{16}$$

And, deviatory stress:

$$r = (9(S*S:S))^{\frac{1}{3}} \tag{17}$$

where $S = stressdeviator = \sigma + pl$. In addition, M-C yield surface is:

$$F = R_{mc}q - p\ tan\ \theta - c = 0 \tag{18}$$

In the given equation, the symbol (R_{mc}),q, p denoted deviatoric stress, Mises equivalent stress and equivalent pressure. $\varnothing(\theta, f^x)$ denoted the friction angle, where θ represented temperature and $f^x, \alpha = 1,2,\ldots$ denoted predefined field variables, and $c(\varepsilon^{-pl}\theta, f^x)$ denoted the evolution of cohesion in the form of isotropic hardening, where ε^{-pl} represented equivalent plastic strain. Table 5 represented the parameters of the backfill material, determined based on the findings of an experimental.

4.5 Characteristics of mortar

In order to accurately predict the behavior of masonry units, it is necessary to consider various types of masonry elements. Utilizing simple micro-modeling (Fig. 5) is an effective approach for achieving this goal. This method involves representing the masonry units using continuous and discontinuous pieces, assuming zero-thickness mortar, and accounting for the interaction between the masonry and mortar. The analysis of mortar

joints and units is conducted independently, with the assumption that they will form a homogeneous composite material with distinct characteristics.

Mortar's cohesive behavior was assessed by analyzing the data presented in Table 6. A "hard" contact condition was applied to ensure the intended behavior of the contact, where "hard" contact denotes interaction without softening or surface penetration within the model. Research findings indicated that the typical coefficient of friction for stone units falls within the range of 0.6 to 0.8, with a value of 0.78 identified as the most representative within this range ((A. Bagherzadeh AZAR and A. SARI 2024; A. S. Amin Bagherzadeh Azar 2024)). This particular value is deemed suitable for the tangential orientation, where a "hard" contact facilitates detachment while preventing intrusion between the elements in the perpendicular orientation. It is posited that the lime mortar showcases cohesive associations, with its cohesive performance delineated by the normal stiffness denoted as K_{nn} and the tangential stiffness represented by K_{ss} and K_{tt}. Evaluation of damage was conducted utilizing stress criteria. The contact was considered as impaired once the tensile and shear stresses reach their peak values f_t and f_s.

5 Blast scenarios

When an explosion occurs under a bridge, the deck is subject to significant uplift forces, which can be exacerbated by the accumulation of pressure in the confined spaces between the span and the abutments. These uplift forces can cause the bridge deck to separate from the interlocking of the spandrel wall and the infill. In the event of explosions above the deck, the combined effects of bending due to local failure can lead to the collapse of one or more spans. The local failure of a span can subsequently lead to neighboring spans being torn from their supports. Explosions below the deck expose the abutments and piers to significant lateral forces that can cause severe deformations, shear, or bending failures. A preliminary risk assessment was conducted to analyze two approaches involving blasts below the deck and above the deck with 100 kg charge weights. As illustrated in Fig. 6 for below deck scenario, the explosive height = 1 m and distance to the piers = 3.13 m, and for above-deck scenarios, h = 1 m and distance to edge of the bridge = 2.53 m.

6 FE model verification

6.1 Artificial strain energy

The hourglass energy serves as a metric for the cumulative artificial load energy in the present study. A lower hourglass energy value signifies a higher level of precision in the numerical simulation outcomes. (Hallquist et al. 1995) suggested that in explosion

Table 6 Mortar cohesive behavior parameters

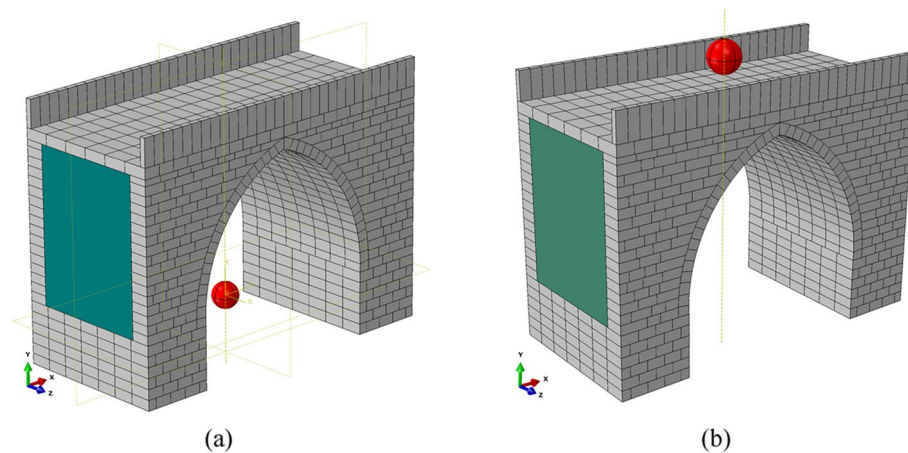| Contact properties								
Tangential	**Normal**	**Cohesive**						
Frication coefficient	Hard contact	Stiffness coefficients (N/m)			Damage			
		K_{nn}	K_{ss}	K_{tt}	Initiation (KN/m²)			Evolution
					Normal	*Shear I*	*Shear II*	Fracture Energy
0.78	-	249.358	95.907	95.907	160	110	274	0.1

Fig. 6 The FE model of explosives for different scenarios; (**a**) below deck explosive location, (**b**) above deck explosive location
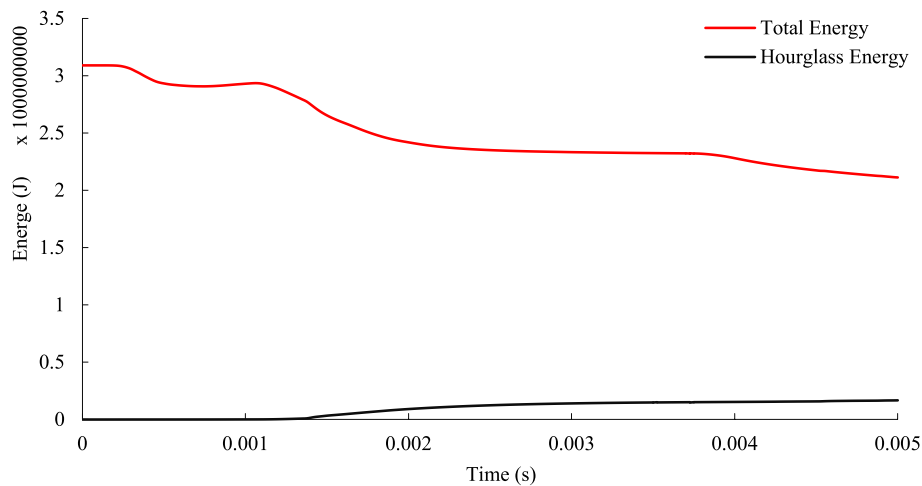

Fig. 7 Energy-time history graph

simulations, the hourglass energy should ideally not surpass 10% of the total energy. As depicted in Fig. 7, the maximum hourglass energy is nearly 0.167E9 J, which accounts for 5.3% in total energy (3.125E9 J). This result verified the accuracy of the simulation model.

6.2 Jone-Wilkins-Lee and Johnson-Holmquist II

As validation for material model, a study carried out by (Liu et al. 2018) was conducted to assess the impact of explosion through field test. The study specifically examined the distortion of a charge hole and two observation holes resulting from the detonation of emulsion explosives on limestone domain. A 3D coupled Euler-Lagrangian finite element model was employed for the validation assessment. The rock area under examination had dimensions of $8 \times 4 \times 5$ m3, while the explosion itself was approximated to have a diameter of 0.11 m and a height of 0.5 m. Jones-Wilkens Lee and Johnson Holmquist-II

model constants was considered for the explosion analysis, over a 2 ms and 0.08 m mesh size. The fracture patterns depicted in Fig. 8 and the extent of the affected area was found to align with the outcomes derived from both experimental and numerical investigations.

7 Result and discussion

The analysis was carried out CEL-FE method with the Abaqus/Explicit solver, known for its computational efficiency compared to the standard solver in terms of time and resource utilization. This solver uses a second-order accurate explicit integration scheme to advance the kinematic state from the previous increment without the need for multiple iterations or solving simultaneous equations. The damping factor was not utilized in the analysis, and the impact of soil was not taken into account. A parametric study was considered on the bridge, with strategically placed TNT charges to analyze deformation, stresses, and damage. The analysis duration was set at 50 ms to ensure the capture of all reflections of the blast wave reaching the bridge. Figure 9 illustrates the propagation of the blast wave over the time for 100 kg of TNT.

Five potential recording locations (Ref-#) were considered for data collection as shown in Fig. 10. Ref-5 is positioned on the inner sides of the pier, Ref-4 was located on the spandrel wall, Ref-3 was placed at the center of the arch, and Ref-2 and Ref-1 were installed below and above the deck, respectively. The identification of scenarios by number and their corresponding locations are indicated in Table 7.

The Von-Mises stress analysis resulting from the detonation of the 1st scenario was presented in Fig. 11a. The highest stress level were recorded by Ref-1 across scenarios 1 to 3 reached at 1E-4 s with an intensity of 2.56E+8 Pa, as illustrated in Fig. 11b. Figure 11c illustrated the displacement in the x-direction for the first scenario, with
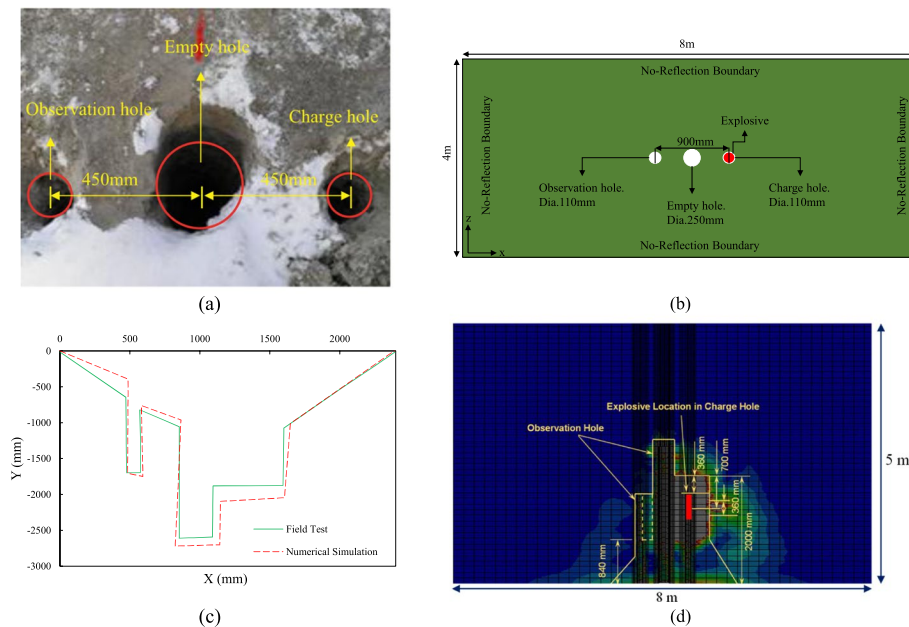

Fig. 8 a Detail of the field test, (**b**) map of the field test in the numerical simulation, (**c**) damage pattern of the field test and (**d**) the numerical simulation and damage zone of the numerical simulation
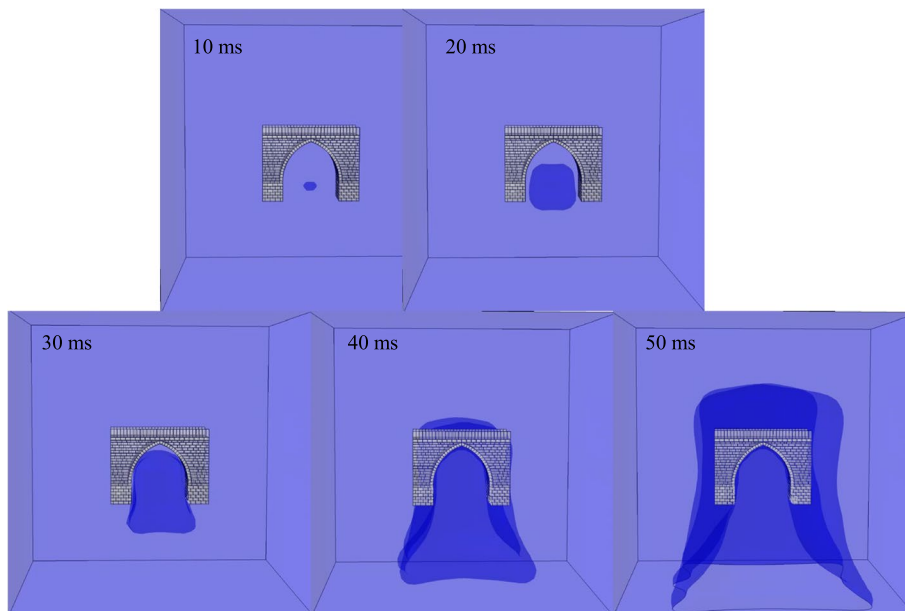
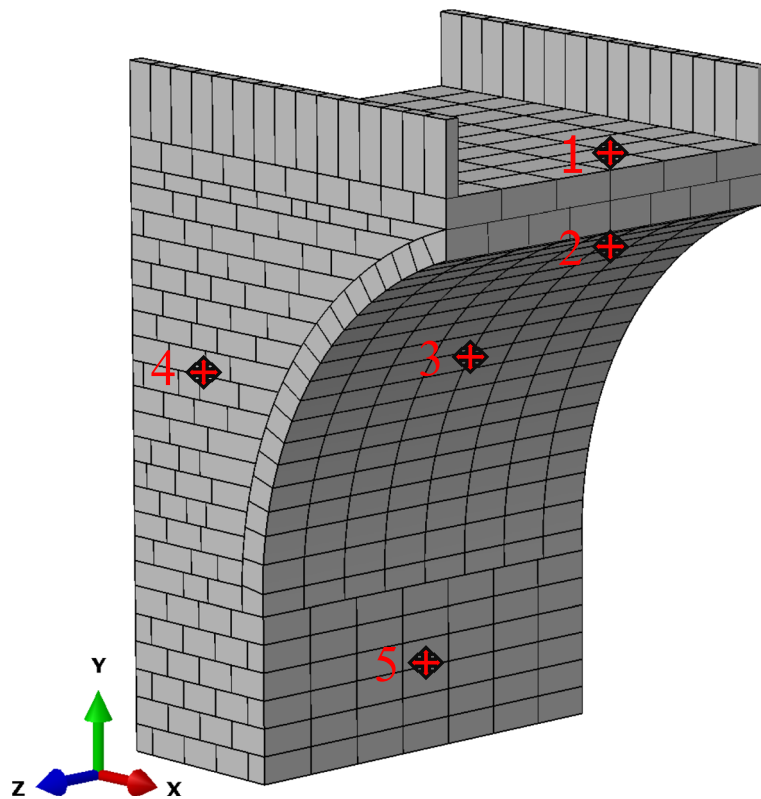**Fig. 9** Blast wave propagation over time for 100 kg trinitrotoluene

Fig. 10 Reference point location
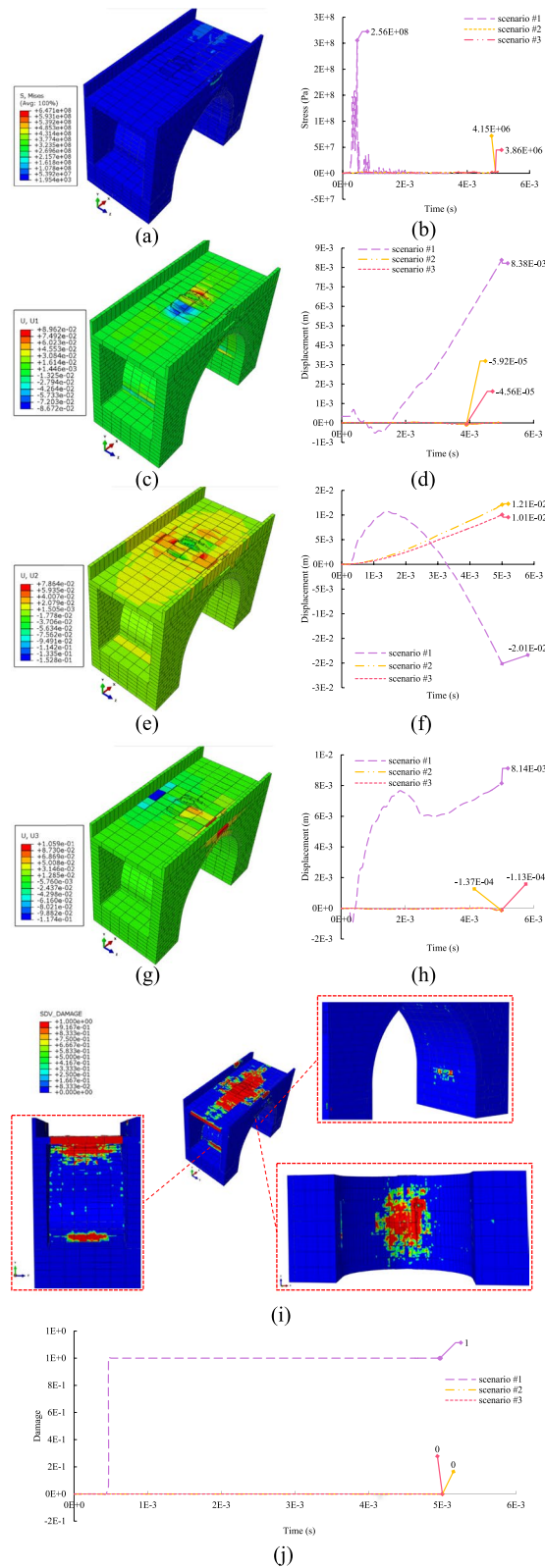
Table 7 Characteristics of the scenarios

Scenario	#1	#2	#3
Location (above/beneath) to deck	above	beneath	beneath (Strengthened)
Weight of charges	100	100	100

the greatest displacement observed at 5E-3 s, measuring 8.38E-3 m recorded by Ref-1 as indicated in Fig. 11d. The y-direction response following the detonation of the first threat scenario was shown in Fig. 11e. The y-direction displacement, recorded by Ref-1 for scenarios 1 to 3, peaked at 5E-3 s with a value of 2.01E-2 m, as shown in Fig. 11f. The response in the z-direction resulting from the detonation of the first scenario was illustrated in Fig. 11g. The displacement in the z-direction, as reported in Ref-1 for scenarios 1 to 3, peaked at 5E-3 s with an amplitude of 8.14E-3 m, as illustrated in Fig. 11h. The structural damage to the overall bridge integrity was minimal during the first scenario, as demonstrated in Fig. 11i. As shown in Fig. 11j, scenario 1 caused local damage to the middle span as recorded by Ref-1, while scenario 2 and 3 has no effect on bridge deck.

The stress analysis results of the detonation in the second scenario were depicted in Fig. 12a, illustrated distribution of Von-Mises stress. The maximum stress level was identified by Ref-2 across scenarios 1 to 3 peaked at 1E-4 s with an intensity of 9.78E+7 Pa, as illustrated in Fig. 12b. Figure 12c illustrated the displacement in the x-direction for the second scenario, with the highest displacement at 5E-3 s, measuring 6.02E-3 m as indicated in Fig. 12d. The y-direction response following the detonation of the second scenario was illustrated in Fig. 12e, where the y-direction displacement peaks at 5E-3 s with a value of 1.26E-2 m, identified by Ref-2 shown in Fig. 12f. The z-direction response resulting from the detonation of the second scenario was illustrated in Fig. 12g, with the z-direction displacement peaking at 5E-3 s with an amplitude of 8.40E-4 m recorded by Ref-2 shown in Fig. 12h. The structural damage to the overall bridge integrity was considered substantial in the second scenario, as illustrated in Fig. 12i. Destruction of the bridge piers, sections of spandrel walls, and arches resulted in breaches in the structure, affecting the piers and leading to a general failure in structural integrity. As shown in Fig. 12j, scenarios 1, 2 and 3 leads to 100%, 36% and 0 damage to the beneath of the deck respectively as recorded by Ref-2.

7.1 Hypothetical reinforcement solutions for Masonry Bridges considering explosion damages

The degradation of the bridge structure, resulting from its behavior and materials, typically appears as cracks, movement, compression, and notable distortion of particular structural elements. Recognizing theoretical hinge points that indicate potential failure modes enables the correlation of transverse cracks with the longitudinal structural performance of the bridge. This connection may suggest insufficient material strength to endure substantial loads or the onset of foundation settlement. The interaction between various parts of a bridge, considering both lengthwise and lateral reactions, may result in structural deterioration that impacts the bridge's overall performance. Strategies for reinforcement include incorporating additional elements into the existing structure to
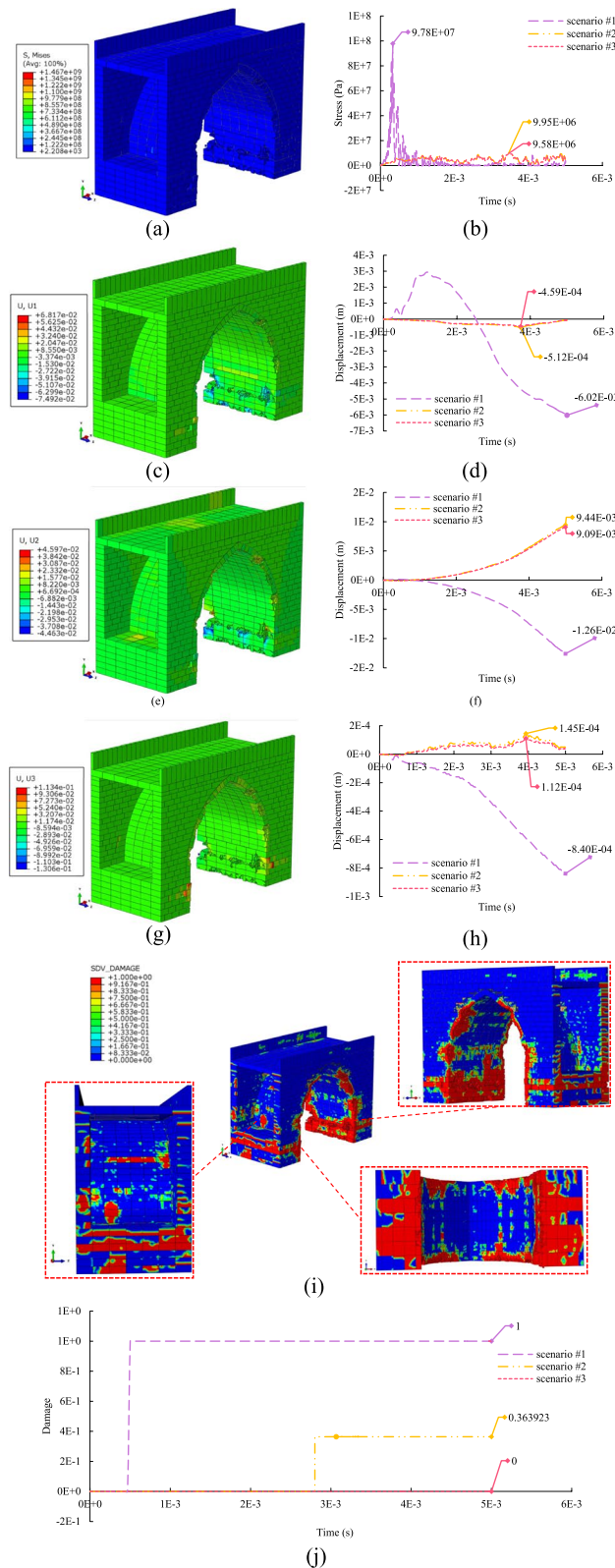
Fig. 11 **a** Von-Mises stress counter of 1st scenario, (**b**) Von-Mises graph of Ref-1, (**c**) U_1 displacement counter of 1st scenario, (**d**) U_1 displacement graph of Ref-1, (**e**) U_2 displacement counter of 1st scenario, (**f**) U_2 displacement graph of Ref-1, (**g**) U_3 displacement counter of 1st scenario, (**h**) U_3 displacement graph of Ref-1, (**i**) Damage counter of 1.st scenario, (**j**) Damage graph of Ref-1

Fig. 12 a Von-Mises stress counter of 2nd scenario, (**b**) Von-Mises graph of Ref-2, (**c**) U_1 displacement counter of 2nd scenario, (**d**) U_1 displacement graph of Ref-2, (**e**) U_2 displacement counter of 2nd scenario, (**f**) U_2 displacement graph of Ref-2, (**g**) U_3 displacement counter of 2nd scenario, (**h**) U_3 displacement graph of Ref-2, (**i**) Damage counter of 2.nd scenario, (**j**) Damage graph of Ref-2

forestall degradation or adapt to shifts in operational circumstances. It is essential to implement these measures with a comprehensive comprehension of the bridge's structure, both before and after any modifications, and to identify existing problems and their root causes while safeguarding the architectural and historical significance of ancient stone bridges. Hence, whenever feasible, it is recommended to adopt methods and remedies that emphasize the retention of the aesthetic charm, structural soundness, and functional utility of the modified bridges. It is crucial to perform a thorough evaluation of the bridge's structure to identify the optimal course of action. The study examined a method to improve the structural integrity of the masonry bridge: incorporating a CFRP composite layers on arches and piers surfaces. The investigation concentrated on scenario #2 (100 kg beneath deck) to reinforce the case study.

Scenario #3 (strengthened bridge in scenario #2) the placement of a 100 kg explosive below the middle of the deck. In this scenario, CFRP strengthening techniques were implemented. The application of these strengthening methods effectively reduced the displacements of the components in all three directions, thereby enhancing the stability and integrity of the bridge. The effect of strengthening techniques on the reduction of displacements for all five reference points (with and without the strengthening techniques) was detailed in Table 8. Moreover, a comparison of the damage counters in Fig. 12i and Fig. 13i indicates a decrease in damages to the piers, arches and spandrel walls in scenario #3 as a result of the strengthening techniques. The stress analysis following the detonation of the 3rd scenario (100 kg beneath the deck) depicted in Fig. 13a, showcasing the Von-Mises stress distribution. The highest stress level documented in Ref-3 for scenarios 1 to 3 peaked at 3.6 E-3 s with an intensity of $4.55E+7$ Pa, as visualized in Fig. 13b. Figure 13c illustrated the displacement in the x-direction for the 3rd scenario, with the maximum displacement occurring at 5E-3 s, measuring 1.43E-3 m for Ref-3 as indicated in Fig. 13d. The response in the y-direction after the detonation of the 3rd scenario was presented in Fig. 13e, with the y-direction displacement reaching its peak at 5E-3 s for Ref-3with a value of 1.97E-3 m, as shown in Fig. 13f. The z-direction response resulting from the detonation of the 3rd scenario was shown in Fig. 13g, with the z-direction displacement peaking at 5E-3 s for Ref-3 with a amplitude of 3.5E-4 m

Table 8 Displacement of reference points with/without strengthening solution

| Ref-1		Ref-2		Ref-3		Ref-4		Ref-5	
x-direction									
WO/STR	W/STR	WO/STR	W/STR	WO/STR	W/STR	WO/STR	W/STR	WO/STR	W/STR
5.92E-5	4.56E-5	5.12E-4	4.59E-4	1.43E-3	9.37E-4	1.12E-4	5.6E-5	1.99E-1	1.24E-1
22.9% Reduction		10.3% Reduction		34.4% Reduction		50% Reduction		37.6% Reduction	
y-direction									
WO/STR	W/STR	WO/STR	W/STR	WO/STR	W/STR	WO/STR	W/STR	WO/STR	W/STR
1.21E-2	1.01E-2	9.44E-3	9.09E-3	1.97E-3	1.93E-3	4.43E-4	4.16E-4	4.99E-2	2.59E-2
16.5% Reduction		3.7% Reduction		2% Reduction		6% Reduction		48% Reduction	
z-direction									
WO/STR	W/STR	WO/STR	W/STR	WO/STR	W/STR	WO/STR	W/STR	WO/STR	W/STR
1.37E-4	1.13E-4	1.45E-4	1.12E-4	1.36E-3	2.58E-5	4.59E-5	4.54E-5	5.38E-3	2.09E-3
17.5% Reduction		22.7% Reduction		81% Reduction		1% Reduction		61.1% Reduction	
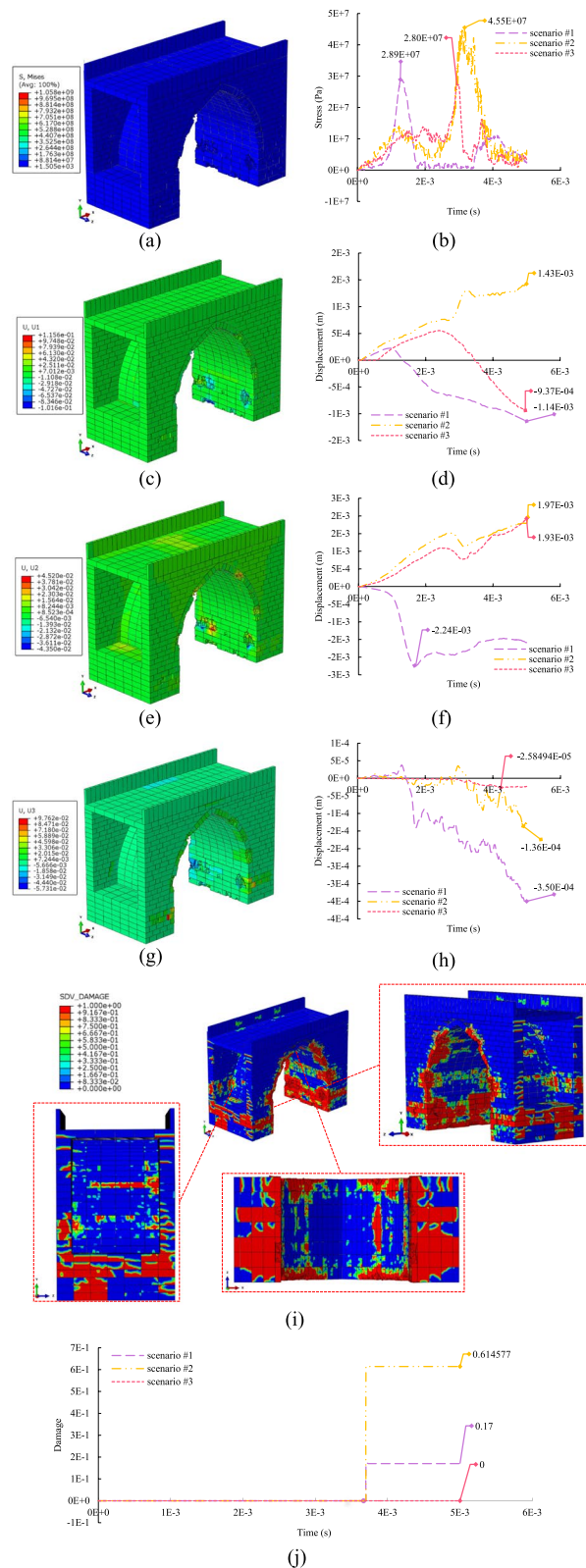
Fig. 13 **a** Von-Mises stress counter of 3rd scenario, (**b**) Von-Mises graph of Ref-3, (**c**) U_1 displacement counter of 3rd scenario, (**d**) U_1 displacement graph of Ref-3, (**e**) U_2 displacement counter of 3rd scenario, (**f**) U_2 displacement graph of Ref-3, (**g**) U_3 displacement counter of 3rd scenario, (**h**) U_3 displacement graph of Ref-3, (**i**) Damage counter of 3.rd scenario, (**j**) Damage graph of Ref-3

depicted in Fig. 13h. The structural damage to the overall integrity of the bridge was deemed significant during this scenario, as evidenced in Fig. 13i. As recorded by the Ref-3 scenario 1 through 3 caused 61%, 17% and 0 damage.

The highest stress level documented in Ref-4 for scenarios 1 to 3 peaked at 4.3E-3 s with an intensity of $1.52E+7$ Pa, as visualized in Fig. 14a. Figure 14b illustrated the displacement in the x-direction recorded by Ref-4 for the all three scenario, with the maximum displacement occurring at 4.12E-3 s, measuring 1.12–4 m. Figure 14c illustrated the y-direction displacement reaching its peak at 4.12E-3 s with a value of 4.43E-4 m for Ref-4. Figure 14d illustrated the z-direction displacement peaking at 4.8E-3 s with a amplitude of 4.59E-5 m for Ref-4 as.

The highest stress level documented in Ref-5 for scenarios 1 to 3 peaked at 2.1E-3 s with an intensity of $3.64E+8$ Pa, as visualized in Fig. 15a. Figure 15b illustrated the displacement in the x-direction for all three scenario, with the maximum displacement occurring at 5E-3 s, measuring 1.99E-1 m. The response in the y-direction after the detonation of the all three scenario was presented in Fig. 15c, with the y-direction displacement reaching its peak at 5E-3 s with a value of 4.99E-2 m for Ref-5. The z-direction response resulting from the detonation of the all three scenario was shown in Fig. 15d, with the z-direction displacement peaking at 5E-3 s with a amplitude of 5.38E-3 m for Ref-5. As shown in Fig. 15e, scenarios 3 which implemented strengthening techniques, resulted in reducing the damage, to the piers surfaces.

8 Conclusion

The impact of explosions on masonry arch bridges can be severe due to the abrupt and intense dynamic loads produced by blast waves. It is essential to comprehend these impacts for the evaluation of structural soundness and the development of suitable mitigation strategies. Explosions emit high-energy shock waves that swiftly travel through the atmosphere. These blast waves impose sudden pressure fluctuations on the bridge framework, resulting in dynamic loading that differs significantly from static loads. The effects
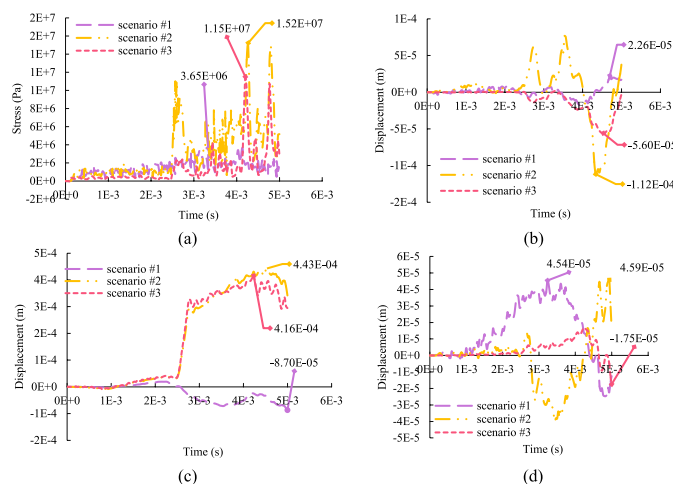

Fig. 14 **a** Von-Mises graph of Ref-4, (**b**) U_1 displacement graph of Ref-4, (**c**) U_2 displacement graph of Ref-4, (**d**) U_3 displacement graph of Ref-4
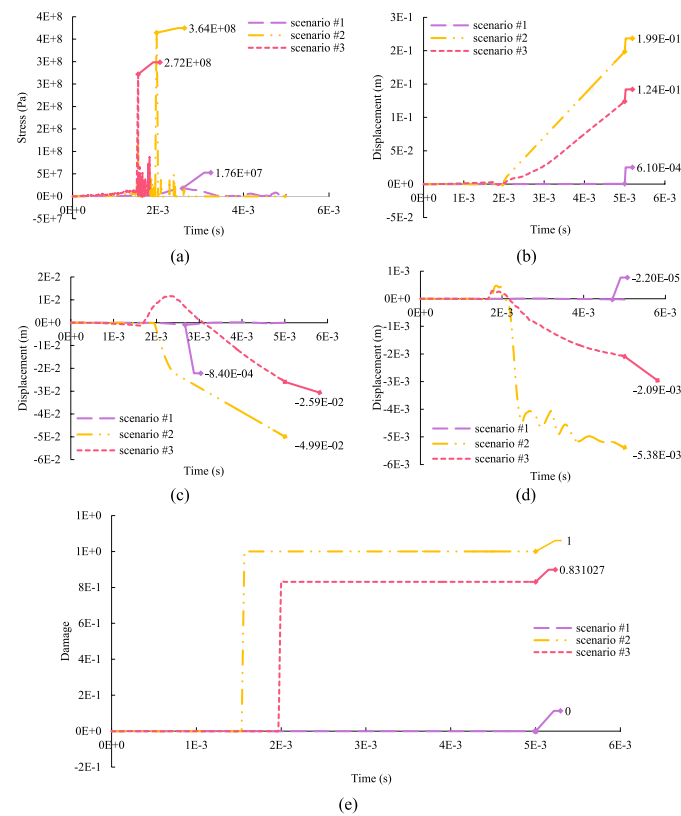
Fig. 15 **a** Von-Mises graph of Ref-5, (**b**) U_1 displacement graph of Ref-5, (**c**) U_2 displacement graph of Ref-5, (**d**) U_3 displacement graph of Ref-5, (**e**) Damage graph of Ref-5

of blast waves include spalling (the detachment of surface layers) and the disintegration of masonry components caused by the swift expansion and contraction of gases within the material. Masonry arch bridges may exhibit fissures in stones, mortar joints, or along the arch due to tensile stresses induced by blast pressures, and substantial explosions can displace stones or entire segments of the bridge, thereby altering its structural stability. The structural behavior of masonry bridges, which are characterized by their arch configuration and construction using stones and mortar, responds dynamically to blast loads. The arch design can magnify stresses and deformations during explosive occurrences, and vibrations triggered by blast waves can induce resonance effects in the bridge structure, resulting in heightened displacements and accelerations. Blast loading has the potential to cause partial or complete failure of the masonry arch bridge, especially if critical structural components such as keystones or springing's are compromised. Blast-induced damage can trigger a progressive failure mechanism in which initial cracks or displacements rapidly spread through the structure under subsequent loading. The analysis of blast effects on stone masonry bridges involves assessing their structural behavior during explosive events. Stone masonry bridges, often possessing historical and structural uniqueness, necessitate meticulous attention and specialized methodologies in blast analysis due to their distinctive material properties and construction techniques. Typically constructed from irregularly shaped stones or bricks bound together with mortar, stone masonry bridges exhibit varying properties such as compressive strength, tensile strength, and density, which

significantly impact their structural response based on the stone type and mortar quality used. Therefore, reinforcement strategies like retrofitting with Carbon Fiber Reinforced Polymer (CFRP) or steel elements may be essential to improve structural capacity and mitigate potential blast repercussions. The application of Carbon Fiber Reinforced Polymer (CFRP) materials can notably enhance the blast resistance of masonry arch bridges owing to their exceptional properties. A below bridge deck explosion can indeed be considered catastrophic, not only due to the immediate damage to the structure but also because of its broader implications for safety, transportation, and the economy in the affected area. Furthermore, when an explosion occurs in a confined space below deck the surrounding structure limits the outward expansion of gases and pressure. This containment can lead to a rapid increase in pressure, which intensifies the explosive force and can cause more extensive damage to the immediate surroundings. Confined spaces can also reflect and amplify the shockwaves produced by the explosion. This phenomenon, known as the "Mach effect," occurs when the shockwaves bounce off walls and surfaces, concentrating energy and causing multiple impacts within the enclosed area. This can lead to structural failure of walls, floors, and ceilings, further exacerbating the damage. The intense forces generated by a confined explosion can compromise the structural integrity of the surrounding walls, floors, and support beams. This can lead to partial or complete collapse of the structure, trapping occupants and hindering rescue efforts. In this study the explosion beneath the deck recognize as the worst scenario and the strengthening technique applied to this scenario, this strengthening technique could significantly reduce the displacement and damage by preventing and limiting cracking and fragmentation of stones and significantly enhance the structural integrity, moreover CFRP providing additional tensile strength and confinement and help reduce the generation of hazardous debris during an explosion. This is critical for the safety of nearby pedestrians, vehicles, and structures. In conclusion, explosions pose significant challenges to the structural integrity of masonry arch bridges due to their unique construction and material properties. Understanding the dynamic nature of blast loading, assessing vulnerability, and implementing targeted reinforcement and repair measures are essential for mitigating the impact of explosions and ensuring the long-term safety and functionality of these historical structures. CFRP materials offer a promising solution for enhancing the blast resistance of masonry arch bridges by improving structural strength, mitigating spalling, and increasing ductility. Proper application techniques and thorough structural analysis are essential to ensure effective and durable reinforcement against blast loading conditions.

9 Nomenclatures

A Intact normalized strength parameter

B Fractured normalized strength parameter

C Strength parameter (for strain rate dependence)

G Shear modulus

D_1 Parameter for plastic strain to fracture

D_2 Parameter for plastic strain to fracture (exponent)

β Fraction of elastic energy loss converted to hydrostatic energy

σ Compressive strength

K_1 First pressure coefficient (equivalent to the bulk modulus)

K_2 Second pressure coefficient

K_3 Third pressure coefficient

HEL Hugoniot elastic limit

P_{HEL} Pressure component at the Hugoniot elastic limit

$\dot{\varepsilon}_0$ Reference strain rate

σ^*_{fmax} Maximum normalized fractured strength

υ Poisson's ratio

M Fractured strength parameter (pressure exponent)

N Intact strength parameter (pressure exponent)

X^T Longitudinal tensile strength

X^C Longitudinal compressive strength

Y^T Transverse tensile strength

Y^C Transverse compressive strength

S^L Longitudinal shear strength

S^T Transverse shear strength;

α Coefficient of contribution of the shear stress to the fiber tensile initiation criterion

$\widehat{\sigma}_{11}, \widehat{\sigma}_{22}, \widehat{\tau}_{12}$ Components of the effective stress tensor

d_f, d_m, d_s Internal (damage) variables that characterize fiber, matrix, and shear damage

Authors' contributions
Conceptualization, A.B. and A.S.; methodology, A.B.; software, A.B.; validation, A.S. and A.B.; formal analysis, A.B.; investigation, A.B.; resources, A.S.; data curation, A.S.; writing—original draft preparation, A.B.; writing— review and editing, A.S.; visualization, A.S.; supervision, A.S.; project administration, A.B. All authors have read and agreed to the published version of the manuscript.

Availability of data and materials
Data available on request from the authors.

Declarations

Ethics approval and consent to participate
Not applicable.

Consent for publication
All the authors have agreed to publish the article in this journal.

Competing interests
The authors declare that they have no conflict of interest.

References
A. BAGHERZADEH AZAR and A. SARI, "Structural Failure of Masonry Arch Bridges Subjected to Seismic Action," *Civ. Eng. Infrastructures J.*, Feb. 2024, https://doi.org/10.22059/CEIJ.2024.366834.1975

A. S. Amin Bagherzadeh Azar, "Damage identification of masonry arch bridge under blast loading using smoothed particle hydrodynamics (SPH) method," *Struct. Eng. Mech.*, 2024, https://doi.org/10.12989/sem.2024.91.1.000.

J. Ali, T. Yehya, K. Jamal, B. Ossama, and K. Said, "The behavior of CFRP strengthened RC beams subjected to blast loading," *Mag. Civ. Eng.*, no. 3 (103), p. 10309, 2021.

A. B. Azar and A. Sari, "Historical Arch Bridges-Deterioration and Restoration Techniques," *Civ. Eng. J.*, vol. 9, no. 7, 2023, https://doi.org/10.28991/CEJ-2023-09-07-010

Bürger D, Rocha De Faria A, De Almeida SFM, De Melo FCL, Donadon MV (2012) Ballistic impact simulation of an armour-piercing projectile on hybrid ceramic/fiber reinforced composite armours. Int J Impact Eng 43:63–77. https://doi.org/10.1016/j.ijimpeng.2011.12.001

Chen P, Wang H, Cao S, Lv X (2022) Prediction of mechanical behaviours of FRP-confined circular concrete columns using artificial neural network and support vector regression: Modelling and performance evaluation. Materials (basel) 15(14):4971

Dong J, Zhao J, Zhang D (2020) Numerical evaluation of reinforced concrete columns retrofitted with FRP for blast mitigation. Adv Civ Eng 2020(1):8884133

Effiong JU, Ede AN (2022) Experimental investigation on the strengthening of reinforced concrete beams using externally bonded and near-surface mounted natural fibre reinforced polymer composites - a review. Materials (basel) 15(17):5848

Hallquist JO, Wainscott B, Schweizerhof K (1995) Improved simulation of thin-sheet metalforming using LS-DyNA3D on parallel computers. J Mater Process Tech 50(1–4):144–157. https://doi.org/10.1016/0924-0136(94)01376-C

Hashin Z, Rotem A (1973) A fatigue failure criterion for fiber reinforced materials. J Compos Mater 7(4):448–464

Hu Y, Chen L, Fang Q, Kong X, Shi Y, Cui J (2021) Study of CFRP retrofitted RC column under close-in explosion. Eng Struct 227:111431

Huang H, Guo M, Zhang W, Zeng J, Yang K, Bai H (2021) Numerical investigation on the bearing capacity of RC columns strengthened by HPFL-BSP under combined loadings. J Build Eng 39:102266

Iqbal N, Sharma PK, Kumar D, Roy PK (2018) Protective polyurea coatings for enhanced blast survivability of concrete. Constr Build Mater 175:682–690

Johnson GR, Holmquist TJ (1999) Response of boron carbide subjected to large strains, high strain rates, and high pressures. J Appl Phys 85(12):8060–8073

Kadhim MMA, Jawdhari AR, Altaee MJ, Adheem AH (2020) Finite element modelling and parametric analysis of FRP strengthened RC beams under impact load. J Build Eng 32:101526

Liu K, Li Q, Wu C, Li X, Li J (2018) A study of cut blasting for one-step raise excavation based on numerical simulation and field blast tests. Int J Rock Mech Min Sci 109:91–104

Liu Y et al (2021a) Blast responses of polyurea-coated concrete arches. Arch Civ Mech Eng 21:1–15

Liu Y, Dong A, Zhao S, Zeng Y, Wang Z (2021b) The effect of CFRP-shear strengthening on existing circular RC columns under impact loads. Constr Build Mater 302:124185

Milad A, Hussein SH, Khekan AR, Rashid M, Al-Msari H, Tran TH (2022) Development of ensemble machine learning approaches for designing fiber-reinforced polymer composite strain prediction model. Eng Comput 38(4):3625–3637

F. Siba, "Near-field explosion effects on reinforced concrete columns: An experimental investigation," Carleton University, 2014.

Swesi AO, Cotsovos DM, Val DV (2022) Effect of CFRP strengthening on response of RC columns to lateral static and impact loads. Compos Struct 287:115356

Tiwary AK et al (2022) Comparative study on the behavior of reinforced concrete beam retrofitted with CFRP strengthening techniques. Polymers (basel) 14(19):4024

Wang P et al (2018) Failure mechanisms of CFRP-wrapped protective concrete arches under static and blast loadings: Experimental research. Compos Struct 198:1–10

Xu JJ, Demartino C, Shan B, Heo YA, Xiao Y (2020) Experimental investigation on performance of cantilever CFRP-wrapped circular RC columns under lateral low-velocity impact. Compos Struct 242:112143

Yan J, Liu Y, Xu Z, Li Z, Huang F (2020) Experimental and numerical analysis of CFRP strengthened RC columns subjected to close-in blast loading. Int J Impact Eng 146:103720

Zhang C, Gholipour G, Mousavi AA (2020) Blast loads induced responses of RC structural members: State-of-the-art review. Compos Part B Eng 195:108066

Publisher's Note